Available online at www.sciencedirect.com

ScienceDirect

Nuclear and Particle Physics Proceedings 273–275 (2016) 250–255

www.elsevier.com/locate/nppp

Point contact germanium detectors at 500 eV_{ee} threshold for light dark matter searches

Arun Kumar Soma, Hau-Bin Li, Shin-Ted Lin, Henry Tsz-King Wong

(on behalf of the TEXONO Collaboration)

Institute of Physics, Academia Sinica, Taipei 11529, Taiwan

Abstract

Germanium detectors with sub-keV sensitivities can probe low-mass WIMP Dark Matter. This experimental approach is pursued at Kuo-Sheng Neutrino Laboratory (KSNL) in Taiwan and at China Jinping Underground Laboratory (CJPL) in China via TEXONO and CDEX programs, respectively. The highlights of R&D efforts on point-contact germanium detectors and in particular the differentiation of surface and bulk events by pulse shape analysis are described. The latest results on WIMP-nucleon scattering cross-sections are also presented. Some of the allowed parameter space implied by other experiments are probed and excluded.

Keywords: dark matter, point contact germanium detectors, surface & bulk events

1. Introduction

There are several compelling evidences from Astrophysics and Cosmology on the existence of dark matter [1] and suggests $\sim$ 27% of universe energy density is comprised by dark matter. The evidences also suggest certain properties of dark matter: non-luminous, non-interacting (electro -magnetic), non-baryonic, non-relativistic (cold) and long lifetime (as of the age of universe). Thus, knowing precise properties of dark matter has evolved into one of the fundamental physics problem of 21^{st} century.

Weakly Interacting Massive Particles (χ, WIMP's) arise naturally in theories beyond Standard Model and are most favored dark matter particles. WIMP's possess above mentioned properties and can be produced in early universe with relic abundance that matches observed dark matter relic density.

The experimental efforts on WIMP's search can be broadly classified into: Direct detection, Indirect detection and Searches at accelerators. The direct searches of WIMP's requires detectors with large mass, ultra low energy threshold at ultra-low background.

The theme of our current experimental research efforts is to deploy germanium detectors with sub-keV sensitivities for light WIMP's direct searches: with the TEXONO [2] and CDEX [3] experiments at Kuo-Sheng Reactor Neutrino Laboratory [4] (KSNL, 28 meter from a 3 GW thermal power reactor core, 30 meter-water-equivalent overburden) and China Jinping Underground Laboratory [5] (CJPL, >2400 m of rock overburden with drive-in access), respectively.

The "baseline design" is: germanium detectors are enclosed by an NaI(Tl) anti-Compton (AC) detector and copper passive shielding inside a plastic bag purged by nitrogen gas evaporated from liquid nitrogen dewar. The set-up is further shielded by copper, boron-loaded polyethylene, steel and lead. At the surface laboratory (KSNL), an additional shielding in the form of cosmic-ray (CR) veto panels comprising of plastic scintillators that are read out by photomultipliers is deployed. The AC and CR detectors are crucial and serve as vetos to reject background and as tags to identify samples for ef-

Email address: arunsoma@mails.phys.sinica.edu.tw (Arun Kumar Soma)

http://dx.doi.org/10.1016/j.nuclphysbps.2015.09.034

ficiency measurements. The details of signal processing and data analysis can be referred to [2, 3, 6].

Point **C**ontact **G**ermanium **D**etection (PCGe) technology (described in Section 2) is being employed for studies on low mass WIMP's. The p-type PCGe (pPCGe) exhibits anomalous surface events behavior that restricts physics sensitivities [6]. The physics origin, separation of bulk from surface events by rise-time measurements along with derivations of efficiency and associated uncertainties are discussed in section 4&5.

To illustrate the analysis procedures in this report, we use 39.5 kg-days of data acquired at KSNL [2, 6] with a 900 g pPCGe whose target is a cylindrical germanium crystal of 60.1 mm in diameter and 60.8 mm in height The application of analysis method on different data set from same detector or other pPCGe detectors gives consistent behavior and results.

2. Point Contact Germanium Detector

The schematic crystal structure of PCGe is depicted in Fig.1. In this configuration capacitance reduces to 1 pF as compared to 20 pF in co-axial configuration and thus resulting in sub-keV energy threshold.

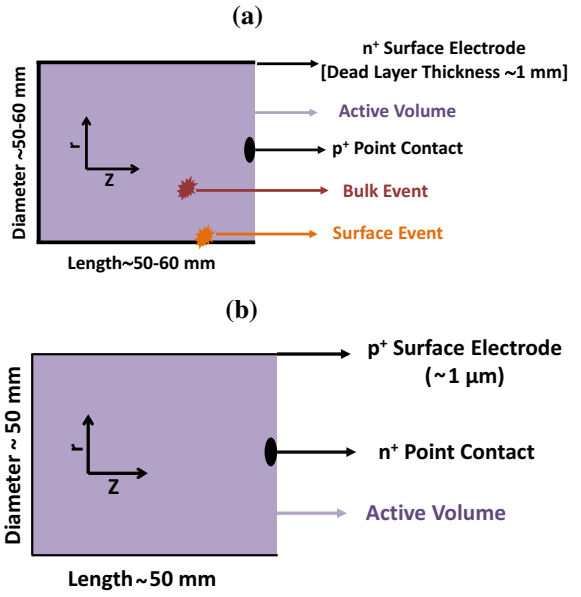

Figure 1: (a) Schematic diagram of pPCGe crystal. (b) Schematic diagram of nPCGe crystal.

The crystal of pPCGE is made of p-type germanium. The outer surface electrode is at positive high voltage towards which the electrons are drifted. The central point contact electrode is at zero-potential. The outer surface electrode is fabricated by lithium diffusion and it's thickness is ~1 mm. The electron-hole pairs produced by radiations at surface (S) layer are subjected to a weaker drift field than those at the bulk (B) region of crystal. A portion of the pairs will recombine while the residual will induce signals which are weaker and slower than those originated in B. Therefore, S-events have partial charge collection and slower rise-time [6].

The pre-amplifiers are coupled to point and surface contact from which electrical signals are extracted. These signals are then processed by shaping and timing amplifiers before feeding to 60 MHz and 200 MHz digitizes, respectively. The process of noise and background suppression are presented in the next section.

The thickness of S layer was measured to be (1.16±0.09)mm by comparing intensity ratios of simulated and observed γ-peaks from ^{133}Ba source [7]. The corresponding fiducial mass for B-region is 840 g.

3. Event Selection

A typical shaping Amplifier (SA) output pulse is shown in Fig. 2. The waveform is characterized by several parameters and some of them are shown in Fig.2. The noise events are then eliminated by exploring correlations between the stored waveform parameters. For example, distribution of pedestal is shown in Fig. 3. The cumulative efficiency of all such cuts (PN:Physics and Noise) is shown in Fig.6c.

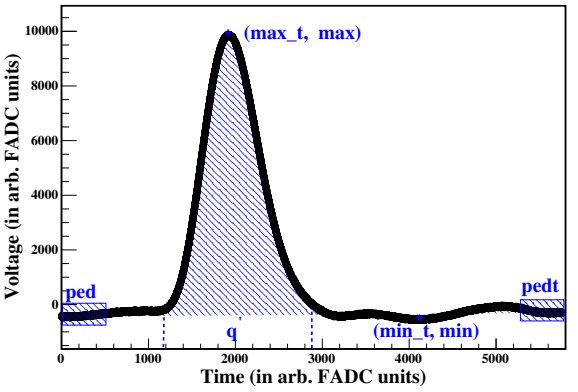

Figure 2: Shaping amplifier (Canberra 2026) output with definitions of some of the analysis parameters.

The energy calibration was performed by using $X-rays$ from ^{68}Ge (10.37 keV), ^{68}Zn (8.98 keV), and $^{68}Ge + {}^{65}Zn$ (1.21 keV) with random trigger events providing zero-energy definition.

The nuclear recoil χN events are uncorrelated with other detector components and are uniformly distributed

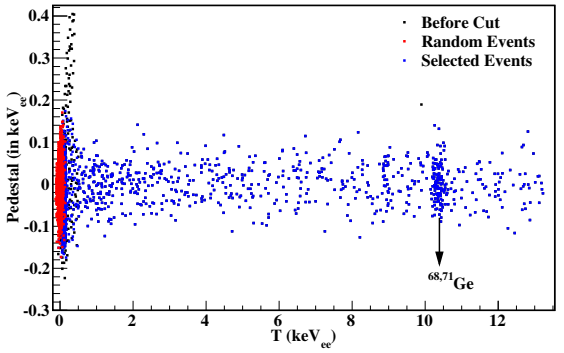

Figure 3: Pedestal fluctuation as a function of T

in pPCGe volume. If superscript $-/(+)$ denotes anti-coincidence (coincidence) of cosmic ray and anti-Compton veto systems with pPCGe signals, then χN events are designated by $AC^{-}\otimes CR^{-}$. The $AC^{+}\otimes CR^{-}$ and $AC^{-}\otimes CR^{+}$ selects ambient gamma and cosmic ray induced high energy neutron events, respectively.

4. Bulk and surface events selection

The typical pulse shape of fast-timing amplifier (TA) are shown in Fig.4. The B&S behavior as described in section 2 is also depicted in Fig.4 a&b at 700 eV_{ee} and 2 keV_{ee}, respectively.

The rise-time of TA pulse were evaluated by using the hyperbolic tangent function:

$$\frac{A_0}{2}\tanh\left(\frac{t-t_0}{\tau}\right) + P_0 \qquad (1)$$

where, A_0, P_0 and t_0 are amplitude, pedestal offset and timing offset, respectively.

P_0 and A_0 are evaluated from the TA-pulses through the difference of asymptotic levels, respectively. The time difference as a function of energy between the TA-edge and the DAQ-trigger instant defined by SA signals is pre-determined, and provides constraints on t_0.

TA amplitude becomes comparable to noise fluctuations at threshold. Therefore, TA pulses were first smoothed by Savitzky-Golay filters [8] with (τ,t_0) as free parameters. The obtained fitting parameters were then employed as initial values to fit raw TA pulses and final fitting parameters were obtained. The smoothed and final fit are shown by blue and red lines in Fig. 4.

The scatter plot of τ versus T for $AC^{-}\otimes CR^{-}$ events is shown Fig.5. A small fraction (<8%) of events at low energy fails the fitting procedures. These events are excluded in subsequent analysis. The signal efficiency is accounted by survival probability of $AC^{+}\otimes CR^{+}$ samples, and is 80% at 500 eV$_{ee}$. Events with τ less(greater) than a selected cut-value τ_0 (=1.23 μs) are categorized as B(S).

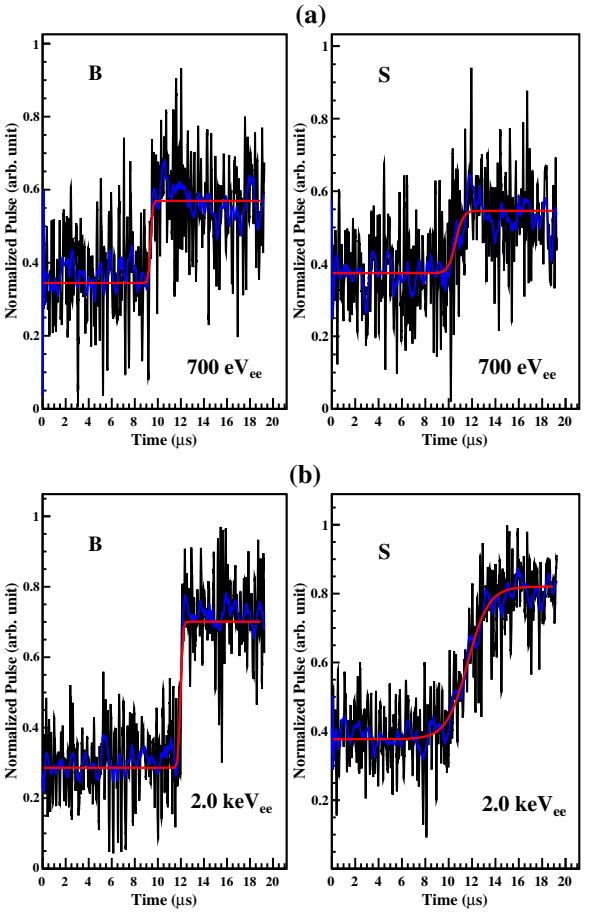

Figure 4: Typical B/S events at (a) 700 $eVee$ and (b) 2 $keVee$ energy, showing the raw (black) and smoothed (blue) pulses, together with the best-fit functions (red).

The width's of measured B and S bands at $T > 1.5$ keV_{ee} is much less than separation of bands from τ_0. Therefore, measured τ provides valid information on locations of events and efficiently differentiate S and B events. This behavior also manifest as distinct two-band structure in Fig.5, with a small fraction (about 8% within 3–6 keV_{ee} of $AC^{-}\otimes CR^{-}$) of events in intermediate transition zone. By studying the corresponding fractions of events with ^{241}Am (<1%) and ^{137}Cs (7.5%) γ-sources, a thickness of 0.16 mm for this zone was derived. The choice of τ_0 is equivalent to defining the spatial borderline between B/S within this transition thickness. This gives rise to a systematic uncertainty in evaluation of pPCGe fiducial mass. It translates to about 3% of total error at 500 eV_{ee}.

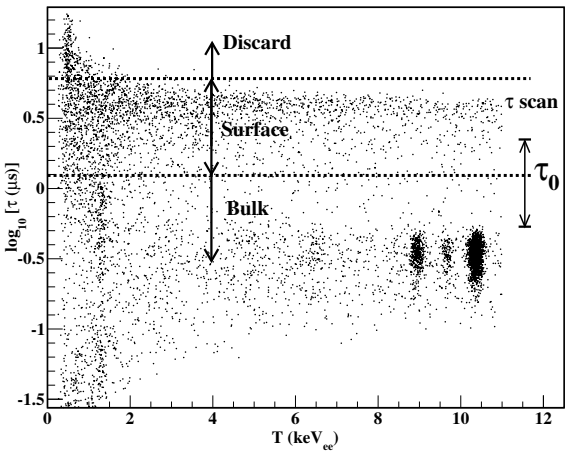

Figure 5: The τ versus T scatter plot for $AC^{-}\otimes CR^{-}$ tags events.

The width's of the measured B and S band at $T < 1.5\ keV_{ee}$ is comparable to band separation and leads to merging of bands. Therefore, there exist contaminations between in B and S events. The evaluation of leakage factors and process to correct the measured spectra are further discussed in the section 5.

5. BS cut Efficiencies Measurement and Correction

The calibration of BS cut requires measurement of bulk signal retaining ($\epsilon_{\rm BS}$) and surface background suppressing ($\lambda_{\rm BS}$) efficiencies. These efficiencies can be obtained by relating the observed (B,S) and actual rates (B_0,S_0) [6].

The normalization assignment (B_0,S_0)=(B,S) is made on events within T_0=2.7-3.7 keV$_{\rm ee}$. It is equivalent to setting $\epsilon_{\rm BS}$ and $\lambda_{\rm BS}$ to 1.0. This energy range is selected because it is above the complications of L-shell X-rays at ∼1 keV$_{\rm ee}$ as well as the physics region in dark matter analysis.

At lower energy, (B,S) and (B_0,S_0) are related by the coupled equations:

$$\begin{aligned} \mathrm{B} &= \epsilon_{\rm BS}\cdot \mathrm{B}_0 \ + \ (1-\lambda_{\rm BS})\cdot \mathrm{S}_0 \\ \mathrm{S} &= (1-\epsilon_{\rm BS})\cdot \mathrm{B}_0 \ + \ \lambda_{\rm BS}\cdot \mathrm{S}_0 \ , \end{aligned} \qquad (2)$$

with an additional unitarity constrain: B_0+S_0=B+S. The derivation of ($\epsilon_{\rm BS}$,$\lambda_{\rm BS}$) therefore requires at least two measurements of (B,S) where the actual rates (B_0,S_0) are known.

The data with ^{241}Am, ^{137}Cs and *in situ* cosmic-ray induced fast neutrons are used for obtaining $\epsilon_{\rm BS}$ and $\lambda_{\rm BS}$.

The chosen three sources plays a complementary role and these data samples are displayed in Fig.6a.

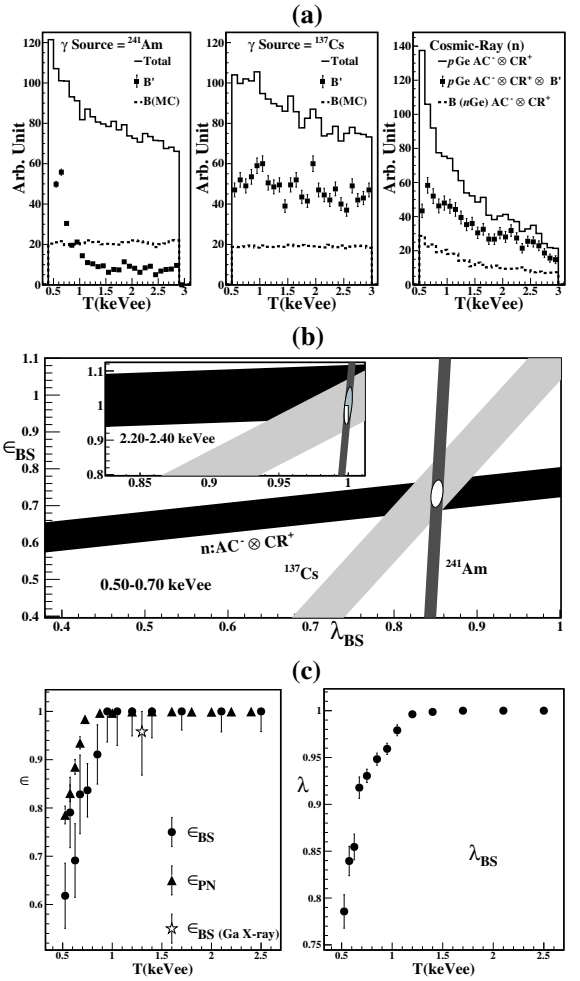

Figure 6: The derivation of ($\epsilon_{\rm BS}, \lambda_{\rm BS}$). (a) The measured Total and B′ spectra from pPCGE with surface-rich γ-ray (^{241}Am, ^{137}Cs) and bulk-rich cosmic-ray induced neutrons. They are compared to reference B-spectra acquired via simulations for γ-rays and nPCGe measurement for cosmic-neutrons. (b) Allowed bands at threshold and at a high energy band. (c) The measured ($\epsilon_{\rm BS}$,$\lambda_{\rm BS}$) and ϵ_{PN} as functions of energy. Independent measurement on $\epsilon_{\rm BS}$ with Ga-L X-rays is included.

(I): Surface-rich events with γ-ray sources − Calibrations with both low and high energy γ-sources (^{241}Am at 60 keVee and ^{137}Cs at 662 keVee, respectively) were performed. As displayed in Fig.6a, the measured B′-spectra are compared to the reference B derived from full simulation with surface layer thickness of 1.16 mm as input. The simulated B-spectra due to external γ-sources over a large range of energy are flat for T<10 keVee.

(II): Bulk-rich events with cosmic-ray induced fast neutrons − A 523 g first-of-its-kind nPCGe detector was constructed. The components and dimensions are

identical to those of pPCGe. The surface of nPCGe is a p^+ boron implanted electrode of sub-micron thickness. There are no anomalous surface effects. Data were taken under identical shielding configuration. The trigger efficiency was 100% above T=500 eVee, and energy calibration was obtained from the standard internal X-ray lines. The $AC^-\otimes CR^+$ condition selects cosmic-ray induced fast neutron events without associated γ-activities, which manifest mostly(~85%) as bulk events. Accordingly, the $AC^-\otimes CR^+$ spectrum in nPCGe is taken as the B-reference and compared with those of $AC^-\otimes CR^+$ in pPCGe.

Using calibration data (I) and (II), (ϵ_{BS},λ_{BS}) are measured by solving the coupled equation 2. Standard error propagation formulae are adopted to derive their uncertainties using errors in (B,B′,S′) as input. As examples, three allowed bands at threshold and at a high energy band are illustrated in Fig.6b. The different orientations of bands are consequences of different depth distributions of the samples, which give rise to different B:S ratios. The bands have common overlap regions, indicating the results are insensitive to event locations. The surface-rich γ-events and bulk-rich cosmic-ray induced neutron-events play complementary roles in constraining λ_{BS} and ϵ_{BS}, respectively. The results are depicted in Fig.6c, with ϵ_{PN} overlaid. By comparing the measured *in situ* Ga-L X-ray peak at 1.3 keVee after BS-selection to that predicted by corresponding K-peak at 10.37 keVee, a consistent ϵ_{BS} is independently measured.

The efficiency-corrected (B_0,S_0) of physics samples can then be derived with the help of measured (ϵ_{BS}, λ_{BS}) by the solution of Equation 2, and is given by

$$\begin{aligned} B_0 &= \frac{\lambda_{BS}\cdot B-(1-\lambda_{BS})\cdot S}{(\epsilon_{BS}+\lambda_{BS}-1)} \\ S_0 &= \frac{\epsilon_{BS}\cdot S-(1-\epsilon_{BS})\cdot B}{(\epsilon_{BS}+\lambda_{BS}-1)} \quad . \end{aligned} \tag{3}$$

The formulae can be understood as: $B_0(S_0)$ should account for loss of efficiency in the measurement of B(S) in the first positive term, followed by a subtraction of leakage effect from S(B) in second negative term.

The $AC^-\otimes CR^-$ tagged events from pPCGe data taken at KSNL at various stages of analysis are depicted in Fig.7a. The measured-B and corrected-B_0 spectra are almost identical at $T > 1.5$ keV_{ee}, this is a direct consequence of $\epsilon_{BS} = \lambda_{BS} = 1$. At low energy, efficiency-correcting and background-subtracting effects compensate each other in this data set.

After subtracting flat background due to high energy γ-rays and known L-shell X-rays contributions predicted accurately by measured higher energy K-peaks, the residual spectrum is shown in inset of Fig.7b.

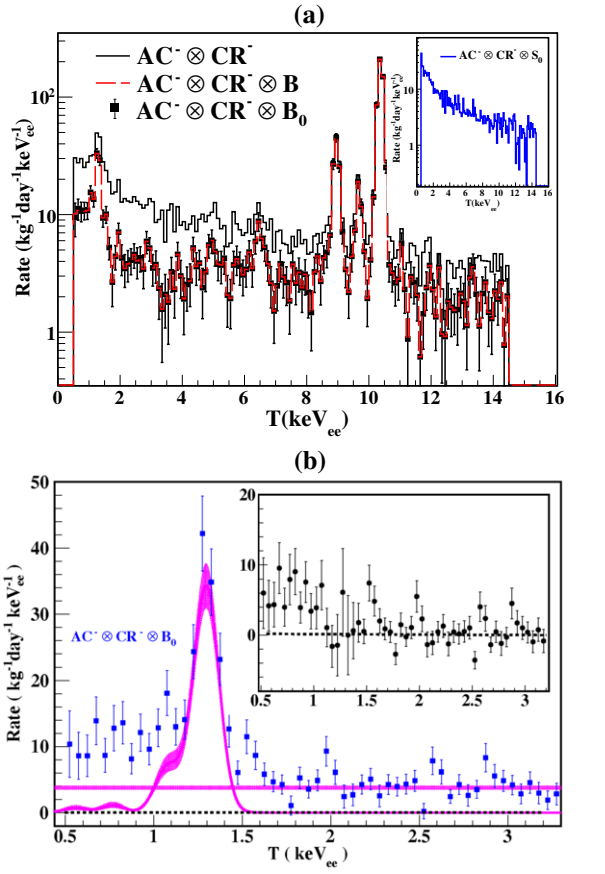

Figure 7: (a) Measured and corrected $AC^-\otimes CR^-$ tag spectra. (b) Shown in magenta are flat background due to high-energy γ-rays from ambient radioactivity, and contributions from the L-shell X-rays. Depicted in inset is the residual spectrum after background subtraction, corresponding to candidate $(\chi/\nu)N$ events.

6. Error Sources and Assignment

The errors on (ϵ_{BS},λ_{BS}) are shown in Fig.6c. They are derived from global fits on allowed bands in Fig.6b. Standard error propagation techniques were applied to derive the resulting uncertainties on (B_0,S_0) via Eq.3.

The uncertainties include contributions from their own measurement errors, (ϵ_{BS},λ_{BS}) calibration errors, as well as systematic uncertainties. Their relative contributions in three representative energy bins are summarized in Table 1. The leading contribution is statistical errors on (B,S), scaled by a factor $1/(\epsilon_{BS}+\lambda_{BS}-1)$. This can be seen from structure of the formulae in equation 3. The total errors therefore increase as ϵ_{BS} and λ_{BS} deviate from unity towards the analysis threshold of 500 eV_{ee}.

Energy Bin	0.50–0.55 keV$_{ee}$	0.95–1.00 keV$_{ee}$	1.90–1.95 keV$_{ee}$
Measurement and Total Error (kg^{-1}keV^{-1}day^{-1})	10.6±5.0	9.8±2.4	6.1±1.6
Relative Contributions to Total Error† :			
I) Uncertainties on Calibration (ϵ_{BS},λ_{BS}) from Fig. 6c :	0.26	0.064	<0.03
II) Measurement Error on B_0 from Eq. 3 :			
Statistical Errors of (B,S)	{ 0.41	{ 0.90	{ 0.99
Scaling by $1/(\epsilon_{BS} + \lambda_{BS} - 1)$	{ 2.29	{ 1.07	{ 1.00
Combined	0.95	0.96	0.99
III) Systematic Uncertainties due to Parameter Choice :			
(i) Rise-time Cut-Value τ_0	0.12	0.25	0.09
(ii) Fiducial Mass from Choice of τ_0	0.03	0.06	0.06
(iii) Normalization Range	{ 0.13	{ 0.10	{ 0.07
(iv) (B_0,S_0)=(B,S) at Normalization	0.08	0.03	0.03
(v) Choice of Discard Region	0.05	0.01	0.001
Combined Systematic Error	0.20	0.27	0.12

Table 1: The contribution of uncertainties on $AC^{-}\otimes CR^{-}\otimes B_0$ spectrum. † Errors are combined in quadrature and total error is normalized to 1.0.

7. Studies on χN spin-independent interaction

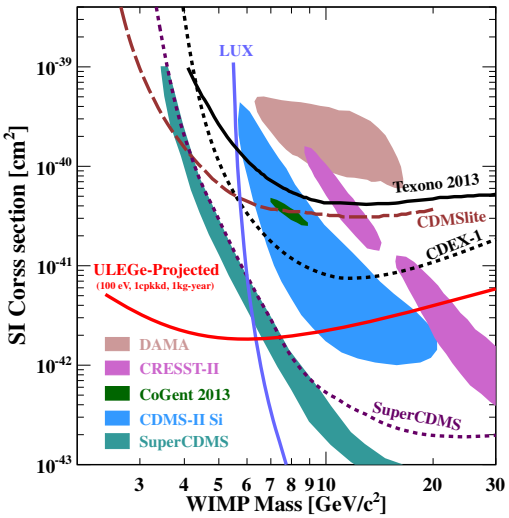

Figure 8: The 90% confidence level upper limit on $\sigma^{SI}_{\chi N}$ from TEXONO, CDEX-1 and other benchmark experiments.

The residual spectrum corresponds to χN candidate events is depicted in inset of Fig. 7b. The Constraints on $\sigma^{SI}_{\chi N}$ were then derived via "binned Poisson" method with conventional astrophysical models[1] (local density of 0.3 GeV/cc and Maxwellian velocity distribution with v_0=220 km/s and v_{esc}=544 km/s). The event rates of χN spin-independent interaction cannot be larger than residual spectrum. The Ge quenching function is derived with TRIM software.

Exclusion plot for $\sigma^{SI}_{\chi N}$ versus m_χ at 90% confidence level from TEXONO [2] and CDEX-1 [3] are displayed in Fig.8, with other benchmark results superimposed[3]. The projected sensitivity at 100 eV_{ee} threshold, 1 kg-Year data size and background at 1 cpkkd is also shown.

8. Conclusion and Future Prospects

A method for evaluating the efficiency and desired correction on obtaining the surface and bulk spectrum is established. Projects on improvement of electronics, sub-noise-edge analysis [10] and scaling up detector mass are being pursued.

9. Acknowledgment

A.K. Soma sincerely thanks ICHEP 2014 for partial financial support towards attending the Conference.

References

[1] M. Drees and G. Gerbier, Review of Particle Physics Phys. Rev. D 86, 289 (2012) and references therein.
[2] S. T. Lin et al., Phys. Rev. D. 79 061101(R) (2009); H.B. Li et al., Phys. Rev. Lett. 110, 261301 (2013) and references therein.
[3] W. Zhao et al., Phys. Rev. D 88, 052004 (2013), Q. Yue et al., arXiv:1404.4946v1 (2014) and reference therein.
[4] H.T. Wong et al., Phys. Rev. D 75, 012001 (2007); M. Deniz et al., Phys. Rev. D 81, 072001 (2010).
[5] K.J. Kang et al., Fron. Phys. China 8(4), 412 (2013); Q. Yue and H.T. Wong, J. Phys. Conf. Ser. 375, 042061 (2012); K.J. Kang et al., J. Phys. Conf. Ser. 203, 012028 (2010).
[6] H.B. Li et al., Astropart. Phys. 56, 1 (2014).
[7] E. Aguayo et al., Nucl. Instrum. Meth. A 701, 176 (2013).
[8] W.H. Press et al., *Numerical Recipes in C*, 2nd ed., Ch.14, Pg.650, Cambridge University Press (2002).
[9] S.T. Lin et al., arXiv:0712.1645v4 (2007).
[10] H.T. Wong, Int. J. Mod. Phys. D 20, 1463 (2011).